A multiscale approach to enhance the thermoelectric properties of α-SrSi2 through micro-/nano-structuring and Ba substitution

Rana Ghannam, Loic Coulomb, Adrien Moll, David Bérardan, David Maurin, Jean-Louis Bantignies, Olivia Mauguin, Antonio Vieira E Silva, Bertrand Rebière, Benjamin Villeroy, et al.

Journal of Alloys and Compounds 1002 (2024) 175422

Contents lists available at ScienceDirect

Journal of Alloys and Compounds

journal homepage: www.elsevier.com/locate/jalcom

A multiscale approach to enhance the thermoelectric properties of α-$SrSi_2$ through micro-/nano-structuring and Ba substitution

Rana Ghannam [a], Loic Coulomb [a], Adrien Moll [b], David Bérardan [b], David Maurin [d], Jean-Louis Bantignies [d], Olivia Mauguin [e], Antonio Vieira e Silva [a], Bertrand Rebière [a], Benjamin Villeroy [c], Jérome Rouquette [a], Geoffroy Chevallier [f], Claude Estournès [f], Romain Viennois [a], Mickaël Beaudhuin [a,*]

[a] ICGM, Univ Montpellier, CNRS, ENSCM, Montpellier, France
[b] ICMMO, Univ Paris Saclay, CNRS, Orsay, France
[c] ICMPE, Univ Paris Est, CNRS, Thiais, France
[d] L2C, Univ Montpellier, CNRS, Montpellier, France
[e] Géosciences Montpellier, Univ Montpellier, CNRS, Montpellier, France
[f] CIRIMAT, Univ. Toulouse, CNRS, Toulouse, France

ARTICLE INFO

Keywords:
Nanostructured materials
Thermoelectric materials
Powder metallurgy
Sintering
Electronic properties
X-Ray diffraction

ABSTRACT

This study investigates the impact of nanostructuring and Ba substitution on the thermoelectric performance and lattice dynamics of cubic $SrSi_2$. The solubility limit of Ba in α-$SrSi_2$ is investigated under varied synthesis conditions, revealing a notable increase beyond previous reports. Mechanical alloying enables a remarkable enhancement, surpassing the conventional solubility limit of 13–14 %at. Ba. After spark plasma sintering (SPS), secondary phases appear above 22 % at. Ba, extending the solubility limit to 22 % at. Ba. High-pressure sintering at 1 GPa further extends this limit to 40 % at. Ba with excellent relative density. Raman and infrared spectroscopy were explored and unveil shifts in lattice dynamics, impacting phonon scattering and indicating a reduction in lattice thermal conductivity. From the electrical resistivity and Seebeck coefficient we were able to determine the evolution of the bandgap with the Ba content which led to an increase of the power factor by about 10 %. Increasing of Ba content also led to a strong decrease of the thermal conductivity leading to an increase of the figure of merit by 68 % compared to pure cubic $SrSi_2$.

1. Introduction

As the global demand for clean and renewable energy continues to escalate, the quest for efficient and environmentally friendly energy conversion methods intensifies. Thermoelectric materials have emerged as frontrunners in this quest, presenting a unique solution by leveraging temperature gradients to generate electricity. Such materials are characterized by their figure of merit ZT such as $ZT = S^2\sigma T/(\lambda_l+\lambda_e)$ with S the Seebeck coefficient, σ the electrical conductivity, λ_L the lattice thermal conductivity and λ_e the electron thermal conductivity.

The ongoing challenge lies in optimizing thermoelectric and thermal parameters, balancing a high Seebeck coefficient with low electrical resistivity and thermal conductivity. To address these challenges, researchers have explored multi-scale thermoelectric materials aiming to reduce thermal conductivity through enhanced acoustic phonon scattering. Various mechanisms, including phonon-phonon, phonon-electron, and phonon-defect scattering, are employed to manipulate phonon propagation and optimize charge carrier concentration [1,2].

In the temperature range of 300 – 500 K, Bi_2Te_3 stands out as the most performing and most used thermoelectric material, consistently achieving ZT values equal to or exceeding 1 [3,4]. However, in the current context, environmental concerns necessitate consideration not only of the figure of merit but also the scarcity, toxicity, and cost of the chemical elements involved [5].

Silicides exhibiting semi-metallic or semiconducting behaviors have garnered significant attention due to their composition from non-toxic, abundant, and economically viable precursors as demonstrated by Mg_2Si, $MnSi_x$ ($1.71 < x < 1.75$), CoSi, $CrSi_2$, $FeSi_2$, SiGe [5–11].

* Corresponding author.
E-mail address: mickael.beaudhuin@umontpellier.fr (M. Beaudhuin).

https://doi.org/10.1016/j.jallcom.2024.175422
Received 18 April 2024; Received in revised form 19 June 2024; Accepted 30 June 2024
Available online 2 July 2024

Among n-type silicides, Mg_2Si-based alloys, particularly $Mg_2Si_{0.7}Sn_{0.3}$ doped with Sb, have shown remarkable thermoelectric performance, achieving ZT values of 0.5 at 300 K and 1.3 at 700 K [5,6]. A recent record was set by $Mg_2Si_{0.7}Sn_{0.3}$ co-doped with Bi and Cr, attaining ZT values of 0.4 at 300 K and 1.7 at 673 K [12]. However, p-type Mg_2Si-based alloys exhibit comparatively lower thermoelectric performance, with ZT values of 0.08 at 300 K and 0.5 at 750 K for $Mg_{1.86}Li_{0.14}Si_{0.3}Sn_{0.7}$ [13]. Notably, the superior p-type silicides are the higher manganese silicides $MnSi_x$ and its alloys [11,14–16]. The most notable properties were achieved in annealed melt-spun Re-substituted HMS, reaching ZT values of 0.2 at 300 K and 1.15 at 873 K [17].

In recent years, $SrSi_2$ has attracted attention for its intriguing thermoelectric properties and stability [18]. Despite this interest, the efforts to enhance its thermoelectric characteristics remain limited in the literature. Until recently, it was thought that $SrSi_2$ crystallizes in two primary phases: the low-temperature cubic phase α and the high-temperature tetragonal phase β [19–21]. The transition between these phases would occur between 450 and 500 °C [19]. However, a recent work has shown that the composition of the tetragonal phase obtained under stable thermodynamic conditions was $SrSi_{1.9}$ instead of $SrSi_2$ and the ordering of the vacancies reduced its symmetry to monoclinic [22]. Therefore, the only way to obtain the stoichiometric tetragonal $SrSi_2$ phase was to use high pressure and high temperature conditions as done previously by Evers [23] or Imai [24] and the cubic phase is congruent with a melting temperature of 1121°C [24]. The cubic phase belongs to either space group $P4_132$ or the enantiomorphous group $P4_332$ [23] with a total of 12 atoms per cell. It is regarded as either a narrow-band gap semiconductor with an energy gap of 35 meV [25,26] or a topological Weyl semimetal with a sharp pseudo-gap in the Fermi level density of states (DOS), as indicated by band structure calculations [27]. However recent results confirmed experimentally that it is a semiconductor ending this controversy [28]. Its power factor $\alpha^2\sigma$ at room temperature (RT) is comparable to the best thermoelectric materials ($\alpha^2\sigma$ = 6–10 $mW.m^{-1}.K^{-2}$ [29,30] for Bi_2Te_3 and Sb_2Te_3 alloys) when it is in its pure form (2.32 $mW.m^{-1}.K^{-2}$ [31]) and even higher when doped with 8 % at. Yttrium (6.23 $mW.m^{-1}.K^{-2}$) [32]. However, its total thermal conductivity remains high (5 – 6 $W.m^{-1}.K^{-1}$) [31–33]. This high thermal conductivity contributes to a figure of merit that is somewhat moderate (0.05 – 0.15 at RT) for pure α-$SrSi_2$ [31–33] but significantly higher (0.4 at RT) when doped with 8 % at. Yttrium. To our knowledge, α-$SrSi_2$ exhibits the highest RT ZT among p-type silicides. Furthermore, DFT calculations predict an optimal ZT of about 0.77 at 300 K and close to 1 at 50 K, indicating the need for further optimization efforts [34].

Various strategies have been employed to enhance the thermoelectric properties of cubic α-$SrSi_2$, including doping to improve both its power factor and phonon scattering through mass defects [35]. These endeavors have resulted in achieving a ZT value of up to 0.4 in α-$Sr_{0.92}Y_{0.08}Si_2$ at room temperature [32]. Despite these promising outcomes, the thermal conductivity remains relatively high (3.8–5 W/m.K), except in defected Ca-alloyed α-$SrSi_2$ where it reaches 2 W/m.K [36]. Two different ways have been followed for reducing the thermal conductivity in undoped $SrSi_2$. Aoyama et al. reported a reduction of the thermal conductivity to about 1 W/m.K at room temperature in a composite thin film of cubic $SrSi_2$ containing some amounts of metastable layered trigonal $SrSi_2$ phase [37]. This led to a rather high ZT of 0.45 at room temperature [37]. Our team has recently followed another way and obtained nanostructured $SrSi_2$ samples after ball milling or melt spinning followed by shaping with the spark plasma sintering (SPS) technique [38]. The thermal conductivity was reduced down to 2.5 W/m.K at room temperature and we obtained a ZT of 0.2 at room temperature for the best sample from ball milling and SPS route [18]. This article explores how to further improve the performances of cubic α-$SrSi_2$ with a multi-scale approach to decrease the thermal conductivity and to optimize the power factor. The substitution of Sr by Ba in cubic $SrSi_2$ has permitted to reduce the thermal conductivity up to 30 % for the highest Ba contents [31,35,39] through increased phonon scattering by point defects. However, different behaviors have been observed for the electronic properties. Singh and Imai [31] and Lue et al. [39] observed a significant increase of the Seebeck coefficient and resistivity in bulk polycrystalline samples whereas Aoyama observed much smaller effect close to the uncertainty of the measurement [40]. These results seem to agree with the opening or increasing of the energy bandgap predicted by the DFT calculations for the Ba substitution in cubic $SrSi_2$ [27]. Lue et al. [39] found first an increase of the power factor by about 60 % for the sample with 7 % at. Ba and then a decrease of the power factor for largest Ba content down to similar values than in pure $SrSi_2$. This result to an increase of the ZT by about a factor 2 up to 0.11 at room temperature for the sample with 7 % at. Ba [39]. Aoyama et al. did not observe a significant change for the power factor with Ba substitution in their thin film [40]. Singh and Imai also observed a slight decrease of the power factor with increased Ba content but the ZT increased from 0.15 to 0.2 [31]. Therefore, further investigations on the effect of Ba on the electronic properties of cubic $SrSi_2$ as well as on its combined effect with the nanostructuring on the thermoelectric properties.

In the present study, the effect of the nanostructuring combined with Ba substitution on the thermoelectric performances of cubic $SrSi_2$ will be presented. We will also study the effect of the Ba substitution on the lattice dynamics of cubic $SrSi_2$.

2. Materials and methods

2.1. Sample preparation

Polycrystalline $Sr_{1-x}Ba_xSi_2$ samples were first synthesized using arc-melting technique with Sr pieces (99.9 %, Neyco) and Si lumps (99.9999 %, Alfa Aesar) in stoichiometric amounts. These polycrystalline $SrSi_2$ alloys were nanostructured using ball milling technique in a Fritsch “Pulverisette 7 premium line” planetary micromill (Fritsch, Idar-obertstein, Germany). A container of 45 mL and seven 10 mm balls both made with tungsten carbide were used as the milling media. The experiment was performed under Ar atmosphere, with a ball-to-powder mass ratio set to 40:1. The speed of the supporting disc and the container were fixed to 850 RPM and 2200 RPM respectively, and the grinding time was fixed to 120 min with 5 minutes cycles milling/pause. After ball milling, Spark Plasma Sintering (SPS) technique was used to prepare dense pellet using a DR Sinter Lab 515 S apparatus (Fuji Electronics, Japan). Tungsten carbide die is used to obtain pellets of 8 mm of diameter and 2 mm of thickness. Uniaxial pressure of 200 MPa and DC pulses were applied at both sides. A dwell time of 5 or 30 min was applied at 800°C. In the case of the $Sr_{0.6}Ba_{0.4}Si_2$ sample, we also shaped it by SPS using a 632Lx SPS apparatus (Fuji Electronics, Japan). A uniaxial pressure 1 GPa was applied and a dwell time of 5 min was applied at 600°C.

2.2. Sample characterization

The samples were analyzed by using a X-Ray Diffraction apparatus Philips X'Pert, CuKα1 and CuKα2 ($\lambda_{K\alpha1}$= 0, 15,406 nm et $\lambda_{K\alpha2}$= 0, 15,444 nm). The XRD patterns were analyzed by pattern matching and Rietveld refinement using the Fullprof software [41]. The crystallite size was determined using the Williamson-Hall formula implemented in the same software using a the pseudo-Voigt Cox-Thompson function with taking in consideration the instrumental broadening obtained using a reference (Y_2O_3 powder annealed at 1400°C for 36 h).

The chemical composition was determined by electron probe microanalysis (EPMA) using a CAMECA SX-A00 instrument equipped with five wavelength-dispersive X-ray spectrometers on 17 points with three standards (Si on Wollas; Sr on $SrSO_4$; Ba on $BaSO_4$).

The Raman spectroscopy was conducted using a Renishaw Invia spectrometer with a wavelength of 633 nm and a resolution of 1 cm^{-1}.

The attenuated total reflectance (ATR) experiments in the far infrared range using a diamond waveguide have been performed with a Brücker IFS66V Fourier Transform Infrared (FTIR) spectrometer equipped with Helium cooled bolometer. The samples investigated by Raman and IR spectroscopies are the pellets obtained by SPS and studied for the thermoelectric properties for the Ba-alloyed samples. The reference $SrSi_2$ sample is a sample obtained by arc-melting for which no secondary phases were observed in XRD experiments.

The total thermal conductivity ($\lambda_{tot} = \alpha dCp$) was derived from the thermal diffusivity α measured by the laser flash method from Netzsch (LFA 457 microflash, Netzsch, Selb, Germany), the density d determined with the Archimedes method and the heat capacity Cp from the Dulong and Petit formula. Electrical resistivity, Seebeck coefficient and Hall effect were characterized with homemade apparatus. The uncertainty values on the Seebeck coefficient, the electrical resistivity, and the thermal conductivity are respectively 6 %, 8 % and 11 % [42]. The electronic contribution to the thermal conductivity was determined with the Wiedemann-Franz Law [43] $\lambda_e = L_0 \sigma T$, with the Lorenz number L_0 equal to [44]:

$$L_0 = 1.49 - 0.49 \quad e^{-|S|/21} + 1.4 \quad e^{-|S|/85} \tag{1}$$

This equation is obtained using the single parabolic band approximation and acoustical phonon scattering.

2.3. Computation details

We have performed the ab initio calculations within the framework of the Density Functional Theory (DFT). The calculations have been performed with the Vienna *ab initio* Simulation Package (VASP) using PAW pseudopotentials and the PBE exchange-correlation functional with [45–47].The energy cut-off was 350 eV and the calculations were converged down to residual forces lower than 10^{-4} eV/Å and with energies lower than 10^{-10} eV. After full structure relaxation, the lattice parameter of cubic $BaSi_2$ was 6.77033 Å, larger than the experimental results (a = 6.715(5) Å [23] 6.72 Å [48] by about 0.8 %. We have used a Monkhorst-Pack [48] generated grid with 15x15x15 k-meshes.

The lattice dynamics calculations were performed with the supercell method implemented in the phonon program of K. Parlinski [49]and using a 2x2x2 supercell with 96 atoms.

3. Results and discussion

The XRD patterns of the $Sr_{1-x}Ba_xSi_2$ alloys after arc melting are given in Fig. 1a. Increasing the amount of Ba leads to an increase of the secondary phases such as β-$SrSi_2$, SrSi and Si up to 22 % at. Ba with nominal stoichiometry due to difficulties in controlling the losses during the arc-melting step. For higher Ba amount one also observes the presence of the $BaSi_2$ orthorhombic phase.

In some previous works reporting synthesis of $Sr_{1-x}Ba_xSi_2$ alloys, the solubility limit of Ba in α-$SrSi_2$ was reported to be x = 0.13–0.14 [33,35, 39,40,50,51]. It is noteworthy that the solubility limit of Ba in α-$SrSi_2$ has been observed to increase in non-equilibrium conditions [31,40,50] Singh et al. [31] achieved an almost single-phase sample of α-$SrSi_2$ with a 19 % at. Ba content by employing spark plasma sintering (SPS) at a pressure of 250 MPa. Aoyama et al. used high-temperature sputtering (650–700 °C) to produce polycrystalline thin films, with the Ba solubility limit measured between 26 % and 29 % at. Ba [40] Evers et al. [50] demonstrated the obtainment of the cubic phase α-$SrSi_2$ for the entire $Sr_{1-x}Ba_xSi_2$ composition range using high-pressure and high-temperature (HP-HT) conditions. Previously, A. Moll et al. [51] successfully stabilized the metastable phase $Ba_{24}Si_{100}$ through mechano-synthesis, which other way only forms under high-pressure and high-temperature (HP-HT) conditions around 1 GPa. It is thus plausible that mechano-synthesis could significantly enhance the solubility limit of Ba in α-$SrSi_2$. This is indeed what is observed in the diffraction patterns shown in Fig. 1b.

We observed that the samples are composed of the α-$SrSi_2$ phase, and no secondary phases are detected in the limit of detection of the equipment up to 40 % at. of Ba. This value is much higher than the solubility limit determined to be about 13–14 % at. by Imai et al. [33] and Lue et al. [39] and can be attributed to the excess of energy provided by the ball milling coupled to the out-of-equilibrium synthesis

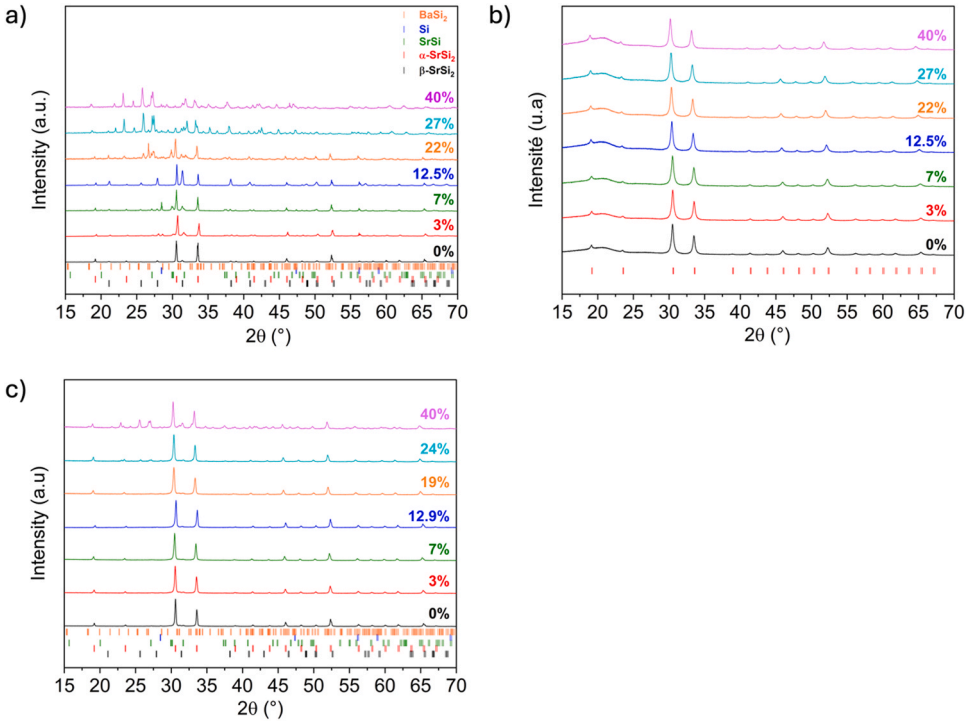

Fig. 1. Diffraction pattern of nanostructured ball milled $Sr_{1-x}Ba_xSi_2$ alloys after a) arc-melting, b) ball milling with nominal stoichiometry and c) SPS sintering (800°C – 200 MPa) with experimental stoichiometry measured by EPMA.

conditions as already observed in several studies [7,8,18,52]. From Rietveld refinement one observes that the unit cell increases with increasing the Ba concentration and follows a Vegard's Law up to 40% at. Ba (See Table 1 and Fig. S1). This result was expected as the covalent radius of Ba (198 pm) is larger than that of Sr (192 pm), suggesting effective replacement of Sr sites by Ba atoms. These observations are in line with the findings of Singh et al. [31], Lue et al. [39], and Imai et al. [33]. In the case of thin films obtained by Aoyama et al., the lattice parameter is slightly smaller (between 6.52 and 6.57 Å), but the trend with Ba substitution remains the same [40]. This difference could arise from the constraints imposed on the silicide film by the Al_2O_3 substrate, which has a smaller lattice parameter.

A significant broadening of the peaks as compared to the arc-melted samples is also observed, which constitutes a signature of a decrease of the crystallite size and an increase of the microstrain. From Williamson Hall formula we determined the crystallite size to be about 75–105 nm and the microstrain between 0.4 % and 0.6 % which is higher than the pure reference sample (about 40 nm). This behaviour could be explained by a change in the mechanical properties of the alloys after Ba substitution although the effect is rather limited.

After SPS sintering (see Fig. 1c and Fig. S2 to S7) traces of secondary phases can be observed as it was the case in pure samples [18]. It could be explained either by an evolution of the samples towards thermodynamic equilibrium, or by the difficulty in detecting very small amount of secondary phases in nanosized powders using XRD. Besides, a narrowing of the Bragg peaks is observed, which indicates an increase of the crystallite size. From Rietveld refinement the amount of secondary phases (β-$SrSi_2$, SrSi and Si) is estimated below 5 % at. for all the composition below 22 % at of Ba. Besides, the orthorhombic $BaSi_2$ is not observable at 22 % at. Ba but appears from 27 % at. Ba. Consequently, we can conclude here that it is possible to extend the solubility limit from 19 % at. [31] to at least 22 % at. For all the samples obtained by this process the relative density is above 98 % which is confirmed by SEM (See Figs. S2 to S7)

The nominal and the experimental composition determined by EPMA are quite similar except for sample $Sr_{0.875}Ba_{0.125}Si_2$ where a higher amount of Sr is measured, probably because of a larger excess added during the arc melting preparation (Table 2). One also observes that there is a slight excess of Ba for low Ba amount and a slight excess of Si for high Ba which is an artefact of the synthesis process and of the loss of alkaline-earth elements during the melting. The crystallite size increases after spark plasma sintering whereas the microstrain decreases. Up to 12.9 % at. Ba the crystallite size increase in the same order of magnitude as in pure α-$SrSi_2$. Above that content, the crystallite size increases much quicker, which precludes reliable microstructural refinements using the Rietveld method. Indeed, it is widely recognized that the determination of crystallite size from XRD experiments using linewidth of the Bragg Peaks is valid up to about 200 nm crystallite size due to the instrumental and resolution limitation although some theoretical works show that it is theoretically possible to determine the crystallite size up to 600 nm – 1 μm [53]. In our case, even in this last case, we are at the limitations of this experimental technique as we estimated crystallite sizes of about 460 nm and 1 μm for 22 % at. Ba and 28 % at. Ba nominal contents, respectively. However, even though no reliable values can be obtained for these compositions, it is possible to conclude with these results that an increase of the Ba concentration does not permit to maintain the nanostructuring to low level.

Table 1
Nominal compositions, phases concentrations and lattice parameters of $Sr_{1-x}Ba_xSi_2$ alloys after mechanical alloying.

Nominal	a (Å)	Crystallite size (nm)	Microstrain (%)
Sr_1Si_2	6.54(6)	45	0.50
$Sr_{0.97}Ba_{0.03}Si$	6.54(8)	106	0.60
$Sr_{0.93}Ba_{0.07}Si_2$	6.55(5)	74	0.60
$Sr_{0.875}Ba_{0.125}Si_2$	6.56(4)	74	0.43
$Sr_{0.78}Ba_{0.22}Si_2$	6.57(9)	78	0.43
$Sr_{0.73}Ba_{0.27}Si_2$	6.59(2)	89	0.43
$Sr_{0.60}Ba_{0.40}Si_2$	6.60(8)	86	0.43

Table 2
Nominal and experimental compositions, phases concentrations and lattice parameters of $Sr_{1-x}Ba_xSi_2$ alloys after SPS.

Nominal	Experimental	a (Å)	Crystallite size (nm)	Microstrain (%)
Sr_1Si_2	$Sr_{1.015}Si_2$	6.5350(1)	211	0.07
$Sr_{0.97}Ba_{0.03}Si$	$Sr_{0.95}Ba_{0.03}$ Si_2	6.5400(0)	114	0.12
$Sr_{0.93}Ba_{0.07}Si_2$	$Sr_{0.94}Ba_{0.07}Si_2$	6.5526(1)	220	0.16
$Sr_{0.875}Ba_{0.125}Si_2$	$Sr_{0.94}Ba_{0.129}Si_2$	6.5581(2)	179	0.05
$Sr_{0.78}Ba_{0.22}Si_2$	$Sr_{0.80}Ba_{0.19}Si_2$	6.5731(0)	-	-
$Sr_{0.73}Ba_{0.27}Si_2$	$Sr_{0.66}Ba_{0.24}Si_2$	6.5891(1)	-	-

To study the effect of high amount of Ba on the thermoelectric properties, we conducted the synthesis of α-$SrSi_2$ with 40 % at. Ba by SPS at a pressure of 1 GPa and 600°C in a tungsten carbide mold with a diameter of 10 mm. The Rietveld refinement performed on this sample is presented in Fig. 2.

The Rietveld refinements indicate that the percentage of the cubic phase is above 95 %, demonstrating that high-pressure sintering has favored the cubic phase and thereby increased the solubility limit of Ba in α-$SrSi_2$ to at least a value of 40 % at. Ba. This agrees with prior Evers's work showing that the complete solubility of Ba in cubic $SrSi_2$ under high pressure and high temperature for P = 4 GPa [43] However, we did not explore higher Ba content with the SPS technique. Crystallite sizes of approximately 125 nm were determined through refinement on these samples, indicating limited grain coalescence. The lower sintering temperature during the SPS process at 1 GPa explain the smaller grain coalescence compared to the other SPS pellets with high Ba content obtained at 200 MPa and 800°C. It is also noteworthy that the microstrain rate is of the same order of magnitude as that obtained under 200 MPa. However, the obtained pellet is cracked, which has limited its characterization to X-ray diffraction (XRD) analyses and Raman spectroscopy.

The evolution of the lattice parameter of $Sr_{1-x}Ba_xSi_2$ alloys after spark plasma sintering (SPS) is depicted in Fig. 3 and follows a Vegard's law up to 40 % at. Ba confirming the substitution of Sr by Ba up to this concentration.

3.1. Lattice dynamics

We have performed Raman spectroscopy and infrared spectroscopy on Ba alloyed $SrSi_2$ samples in order to study the influence of Ba content on the lattice dynamics of cubic $SrSi_2$.

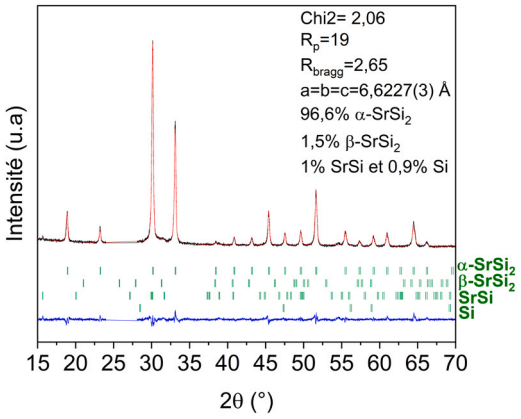

Fig. 2. X-Ray diffractogram of $Sr_{0.6}Ba_{0.4}Si_2$ obtained after sintering at 1 GPa. The 24 – 27° section was removed for Rietveld refinement as it corresponds to the peak of carbon residue from the SPS process.

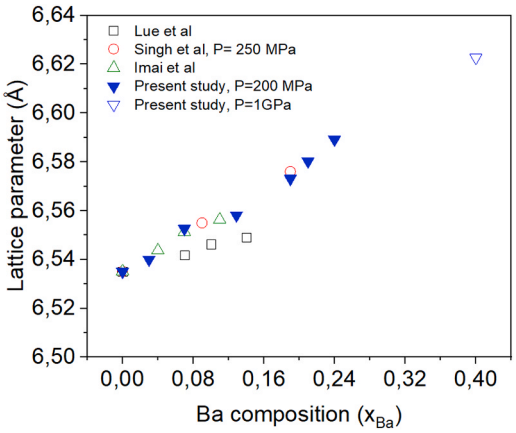

Fig. 3. Lattice parameter of SPS samples as a function of the measured composition of Ba and compared to the literature [17,19,25].

As reported in our previous work [14], the decomposition of the vibrational in irreducible representation in cubic $SrSi_2$ is as follow:

$$\Gamma = 1A_1 \oplus 2A_2 \oplus 3E \oplus 4T_2 \oplus 5T_1$$

Among these vibrational modes, there are 4 IR-active modes ($4T_1$) and 8 Raman-actives modes ($1A_1 \oplus 3E \oplus 4T_2$), and 2 hyper-Raman-active modes ($2A_2$). The acoustic phonons (3 acoustic phonons in total) have T_1 symmetry.

In our previous Raman scattering experiments, 7 Raman-active modes among the 8 expected modes were observed, the last one being superposed to another Raman-active mode as indicated by our calculations on pure cubic $SrSi_2$ [18]. In our present work, because the two lower energy Raman-active are weak, we were able to follow only the 5 Raman-active modes above 150 cm^{-1}. However, it was not possible to reliably determine the positions of the shoulders at about 220 cm^{-1} in the Ba alloyed samples because of the background in this spectral range. Our ATR experiments in the far infrared range are the first ones reporting the IR-active modes in cubic $SrSi_2$ and its alloys. Unfortunately, in pure cubic $SrSi_2$, we were able to observe only one of the four IR-active mode at 201 cm^{-1}. This frequency was slightly larger than in the DFT calculations, as it is also the case for the Raman-active modes. This is due to the overestimation of the lattice parameter in DFT calculations as discussed in [14].

An increase of the Ba content leads to a shift of the Raman lines towards the lower wavenumber, which is directly related to the increase of the lattice parameter due to the increase of the atomic radius of the Ba compared to Sr. One also notices a broadening of the lines (e. g. the FWHM of the line at about 400 cm^{-1} increases from 7.5 cm^{-1} in pure $SrSi_2$ to 20–30 cm^{-1} in the Ba substituted samples), which could be due to either an inhomogeneous disorder or a possible signature of an increase of the phonon scattering. Consequently, in all cases, a decrease of the lattice thermal conductivity with increasing the Ba content can be expected. In the case of the IR-active modes, one observes the signature of a second IR-active mode at about 135 cm^{-1} when alloying with Ba atoms. This is corroborated by our DFT calculations predicting an IR-active mode at about 128 cm^{-1}. We note the presence of several broad and weak features at about 160, 220 and 260 cm^{-1} for the two samples with 19 % at. and 40 % at. of Ba but not in the other samples. Their origin is not clear. The Fig. 5 gives the evolution of the frequencies of the different Raman-active and IR-active modes with the amount of Ba. One can see that the frequencies of the IR-active modes decrease with increasing Ba content as in the case of most of the Raman-active modes. In contrast, the frequency of the IR-active mode at about 200 cm^{-1} increases with Ba content. We also report in the Table 3 the frequencies of the Raman active modes of cubic $SrSi_2$ obtained from our Raman scattering experiments and with our prior DFT calculations [18] for comparison with the frequencies of the Raman active modes of cubic $BaSi_2$ from our present DFT calculations and previous Raman scattering experiments [54,55]. We observe that the vibration frequencies of the Raman-active mode above 300 cm^{-1} decrease significantly when Sr is replaced by Ba, as confirmed by the DFT calculations and is consistent with our Raman scattering experiments on $Sr_{1-x}Ba_xSi_2$ alloys. However, the IR-active mode at about 200 cm^{-1} increases with Ba content, as confirmed by the DFT calculations. This agrees with our experimental observations on $Sr_{1-x}Ba_xSi_2$ alloys. For the Raman-active modes at about 165 cm^{-1}, we observe a slight decrease of the frequencies with Ba content in our Raman scattering experiments in agreement with the DFT calculations but in disagreement with prior experiment on cubic $BaSi_2$. We have no explanation for such disagreement. The DFT calculations predict a decrease of the frequencies of the two lower energy IR-active modes when Sr is replaced by Ba, in agreement with our experimental observations on $Sr_{1-x}Ba_xSi_2$ alloys for the IR-active mode at about 135 cm^{-1}. The above observations are not surprising as the Grüneisen parameters γ_i^T which are relied to volume dependence of the vibration frequencies, are much higher for the Raman-active modes above 300 cm^{-1} than for the modes between 150 and 300 cm^{-1} [18,56].

3.2. Thermoelectric properties

The temperature dependences of the Seebeck Coefficient and electrical resistivity are given in Fig. 6. The positive sign of the Seebeck coefficient confirms the p-type character of the compounds, as hole-type carriers dominate the electrical transport. This observation is consistent with the presence of a small hole pocket in the vicinity of the Fermi level, in agreement with the study of Singh et al. and Lue et al. [31,39]. We observe an increase of the Seebeck coefficient with the Ba content, in agreement with the study of Singh et al. and Lue et al. [31,39]. This is in contrast to the lack of a clear trend observed by Aoyama et al. for the Seebeck coefficient at room temperature in thin films of $Sr_{1-x}Ba_xSi_2$ [40].

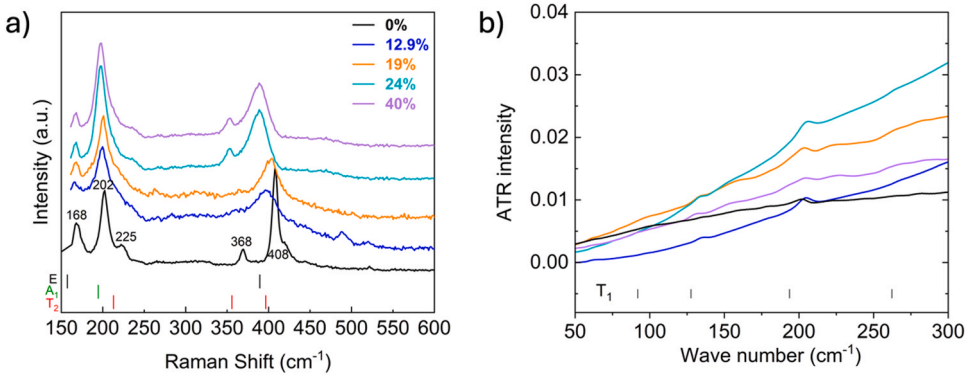

Fig. 4. a) Raman spectra and b) ATR spectra of $Sr_{1-x}Ba_xSi_2$ samples at room temperature.

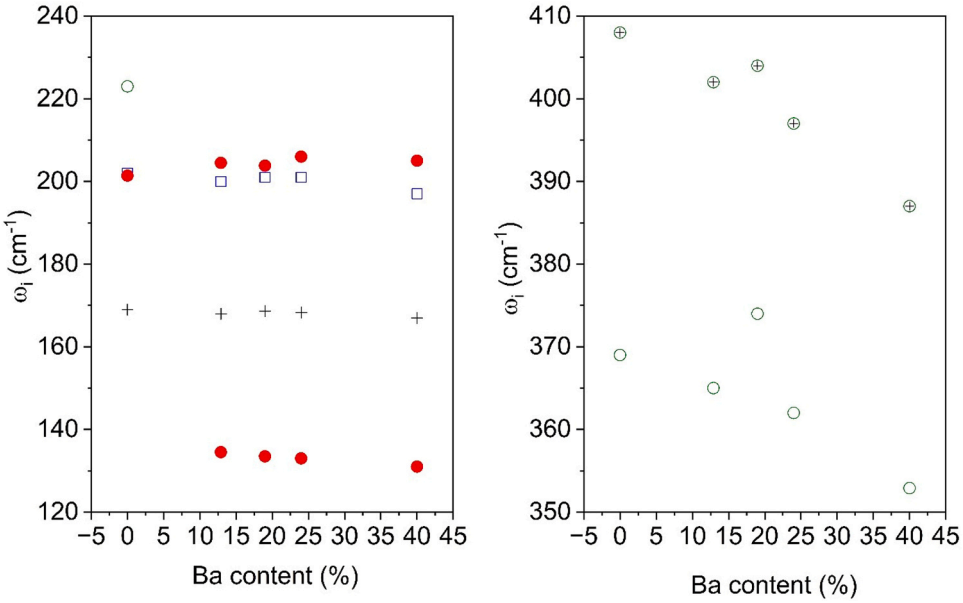

Fig. 5. Raman and IR active modes frequencies (green hollow circle = T_2, red full circle = T_1, blue full square = A_1, black cross = E).

Table 3
Experimental (present work) and theoretical [14] symmetries and frequencies (in cm^{-1}) of the vibrational modes of α-$SrSi_2$ compared with experimental [54,55] and theoretical (present work) symmetries and frequencies (in cm^{-1}) of the vibrational modes of cubic $BaSi_2$. The Raman active modes and infrared active modes are labeled with R and I, respectively.

Symmetry	$SrSi_2$ DFT [14]	$SrSi_2$ exp.	$BaSi_2$ exp. [54]	$BaSi_2$ exp. [55]	$BaSi_2$ DFT
A_2	60				53.8
T_1 (I)	91.9				80
E (R)	96.2	103[a]			78.2
T_2 (R)	117.1	123[a]			95
T_1 (I)	127.7				118
E (R)	157.3	169		168	161.3
A_2	168.2				191.1
T_1 (I)	193.6	202			204.7
A_1 (R)	194.6	203	207	205	199.2
T_2 (R)	213	223	220	232	226.7
T_1 (I)	262.3				238.4
T_2 (R)	355.8	369			317.6
E (R)	389.5		316	331	332.5
T_2 (R)	396.6	408	338	354	339.2

However, we have observed a slight decrease in the Seebeck coefficient for x = 0.129, for which the EPMA data are not in accordance with the nominal composition, we do not have explanations. As can be seen in the Fig. 6, the Seebeck coefficient decreases as the reciprocal temperature in a significant temperature range. This should be due to thermal activation of the intrinsic charge carriers due to the narrow bandgap.

In the case of nondegenerate intrinsic semiconductor and assuming parabolic band, one can determine the energy bandgap through [57]:

$$S = \frac{k_B}{e}\left(\frac{E_F - E_V}{k_B T} + B\right) = \frac{k_B}{e}\left(\frac{E_g}{2k_B T} + B\right) \quad (2)$$

with k_B the Boltzmann constant, e the electron charge, E_F the Fermi energy, E_V the energy of the valence band edge, B is a constant related to the scattering parameter and E_g the energy bandgap. In this case, for $SrSi_2$, one obtains an energy bandgap of 32.3 meV, in close agreement with the value found by Hall effect by Imai et al. (35 meV) [26] and between the values found with the electrical resistivity by Singh and Imai (25 meV) [31] and Imai et al. (43 meV) [33].

One also notices that the electrical resistivity increases with increasing the Ba content (except again for x = 0.129) and that an intrinsic semiconducting behavior appears in the whole temperature range for high amount of Ba Singh and Imai [31] also observed an increase of the electrical resistivity with the amount of Ba above 300 K, however if we have a look to the work of Imai et al. [33], Lue et al. [39], and Aoyama et al. [31] who studied these compounds below 300 K, there was no clear tendency. The energy bandgap obtained from the Seebeck coefficient from the Eq. 2 are shown in the Fig. 6 together with prior results obtained from Hall effect for $SrSi_2$ [26] and for the $Sr_{1-x}Ba_xSi_2$ alloys from electrical resistivity [31,33]. One finds larger energy bandgap from the Seebeck coefficient than from the electrical resistivity, but the general tendency is an increase of the energy bandgap with the Ba content. Notice that the variation of E_g can be attributed to slight uncertainty on the Seebeck coefficient.

We also notice that for Imai et al. [33] an increase of activation energy was observed from the electrical resistivity measurement when the Ba content increase, whereas a previous work from the same team observed a decrease of the activation energy with the pressure, i.e. with volume decrease [31]. For the alloys with x = 0.037 and 0.07, they found values of the energy bandgap close to those we found from the Seebeck coefficient. More recently, Singh and Imai also confirmed an increase of the activation energy with increasing the Ba content [31] and they found values of the energy bandgap close to those we found from the electrical resistivity. Consequently, all these results and our own results shows that the activation energy and the band gap increase with increasing the volume of α-$SrSi_2$. Recently, ab-initio calculation confirmed this behavior [27]. This increase will favor the semiconducting behavior of the alloys which will permit to increase both the electrical resistivity and the Seebeck coefficient with the increase of Ba, which is in adequation with our current case. As can be seen in the Fig. 7, a maximum power factor of 1.38 $mW.m^{-1}.K^{-2}$ was obtained at room temperature for the different composition which corresponds to an improvement of 10 % compared to pure α-$SrSi_2$.

From Fig. 7, one notices the general tendency of a decrease of the thermal conductivity increasing the amount of Ba at the exception of the composition x = 0.129 which is similar to that of 3 % at. Ba. However, it is important to notice that the variations are in the 11 % error bar expected for such measurement, which does not permit to give any conclusion on this unexpected behavior. A minimum total thermal conductivity of approximately 1.96 $W.m^{-1}.K^{-1}$ at room temperature was achieved for x = 0.24, representing a 40 % decrease compared to

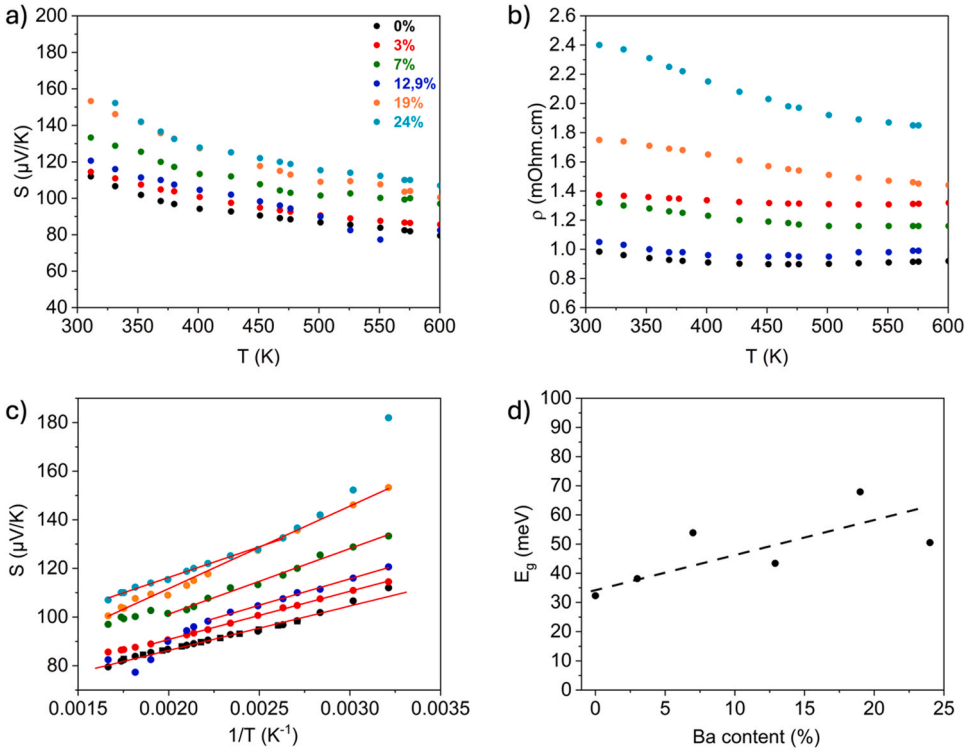

Fig. 6. a-c) Thermal variation of the Seebeck coefficient and of the b) electrical resistivity, d) Energy bandgap of the $Sr_{1-x}Ba_xSi_2$ alloys obtained from the Seebeck coefficient.

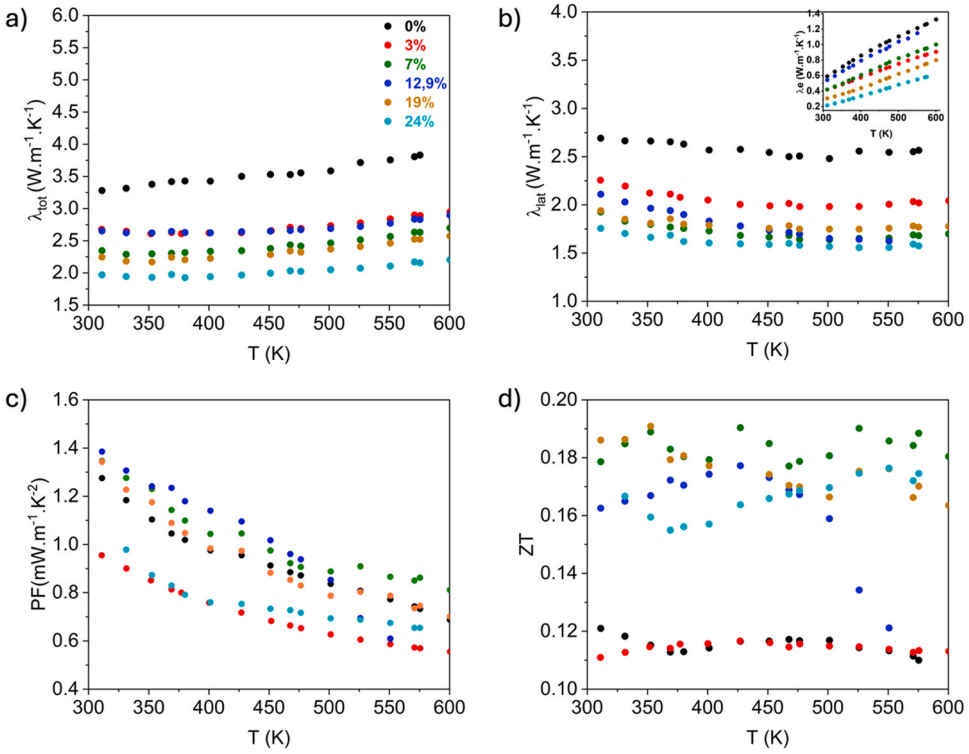

Fig. 7. a) Total thermal conductivity, b) electronic and lattice thermal conductivity and c) Power factor and d) Figure of merit of $Sr_{1-x}Ba_xSi_2$ alloys.

the undoped pure alloy (3.28 $W.m^{-1}.K^{-1}$). This reduction stems from both a decrease in electron contribution and a decrease in lattice thermal conductivity, which diminishes by 35 % in this case. Comparing these values to those reported in the literature at room temperature, Lue et al. [39] obtained a minimum thermal conductivity of around 3.5 $W.m^{-1}.K^{-1}$ with x = 0.14, and Singh et al. [31] achieved a slightly lower total thermal conductivity of 2.9 $W.m^{-1}.K^{-1}$ for x = 0.19, slightly higher than the value obtained for the same concentration in our study (2.24 W/m

K). Since our sample exhibits the same electronic thermal conductivity as their sample (0.3 W/m K at 300 K), the difference arises solely from the lattice thermal conductivity, which is 25 % lower in our sample. This deviation could be attributed to the nanostructuring by mechanical milling of our alloys. It is noteworthy that the total thermal conductivity experiences a slight increase at high temperatures for all $Sr_{1-x}Ba_xSi_2$ alloys and that the measurement are reproducible when the temperature decreases. This upward trend is also observable in the lattice thermal conductivity. Indeed, whereas the lattice thermal conductivity would be expected to decrease due to Umklapp scattering, it is mainly constant suggesting the presence of a bipolar contribution consistent with the narrow bandgap.

Regarding the electronic thermal conductivity, it decreases as the Ba concentration increases. This result aligns with the trend observed in the Seebeck coefficient and charge carrier concentration. Ultimately, it is noteworthy that the ZT for nanostructured $SrSi_2$ increased by 68 % with the substitution of 7 % at. Ba. A maximum ZT of approximately 0.19 was thus achieved at room temperature for the sample with $x = 0.19$, but the highest average ZT of 0.18 in the 300–575 K range was observed for the sample with $x = 0.07$. Comparing this with the pure compound (ZT = 0.05) [13,32], we observe an approximately 140 % increase in the ZT and about 68 % increase for nanostructured pure compound. However, it is important to note that this value is close to the ZT obtained by Singh et al. [31] of about 0.21 with 19 % at. Ba and is higher than that obtained by Lue et al. [39] who achieved a maximum ZT of 0.11 with 7 % at. Ba.

Therefore, we conclude that nanostructuring combined with Ba substitution reduces further the thermal conductivity up to almost 40 % but enhances only slightly the thermoelectric properties of the α-$SrSi_2$ alloy mainly because of the strong increase of the electrical resistivity for high Ba contents. Additionally, the only explanation that accounts for the differences with Singh's work may concerns the purity of the starting elements or the synthesis conditions. Indeed, we noticed in our previous work [13] that the use of 2 N or 3 N Sr leads to strong modification of all the thermoelectric properties.

4. Conclusion

The solubility limit of Ba in α-$SrSi_2$ was explored, revealing an increase up to 40 % at. under non-equilibrium conditions than previously reported solubility limits. The substitution was confirmed with the Vegard's Law. After spark plasma sintering (SPS) under standard conditions the solubility limits extend up to 22 % at. Ba, above this amount, secondary phases are observed. However, using high-pressure sintering at 1 GPa we showed that it is possible to extend the solubility limit up to 40 % at. Ba with a relative density above 98 %. Raman and infrared spectroscopy reveal changes in lattice dynamics with Ba content, influencing phonon diffusion and suggesting a decrease in lattice thermal conductivity. The Seebeck coefficient increases with Ba content. Combined with electrical resistivity measurement we were able to determine the behavior of the energy bandgap which indicates that it increases with Ba content. The power factor after Ba substitution improves by about 10 % for 7 % at. Ba compared to pure α-$SrSi_2$.

Total thermal conductivity decreases with increasing Ba, with a minimum achieved at 1.96 $W.m^{-1}.K^{-1}$ for $x = 0.24$. The deviation from literature values is attributed to nanostructuring. Electronic thermal conductivity decreases with Ba concentration, aligning with Seebeck coefficient trends. The ZT value increases by 140 % with 8 % at. Ba substitution, reaching approximately 0.19 at room temperature. Nanostructuring combined with Ba substitution significantly reduces thermal conductivity but only slightly enhances thermoelectric properties, primarily due to increased resistivity at high Ba contents. Discrepancies with previous works are attributed to the purity of starting elements.

CRediT authorship contribution statement

David Berardan: Writing – review & editing, Validation, Resources, Investigation, Formal analysis. **David Maurin:** Validation, Resources, Investigation, Formal analysis. **Bertrand Rebière:** Formal analysis, Investigation. **Jean-Louis Bantignies:** Writing – review & editing, Validation, Resources, Investigation, Formal analysis. **Olivia Mauguin:** Validation, Resources. **Antonio Vieira e Silva:** Validation, Resources. **Benjamin Villeroy:** Validation, Resources. **Jérome Rouquette:** Validation, Formal analysis. **Geoffroy Chevallier:** Validation, Resources. **Claude Estournès:** Writing – review & editing, Validation, Resources, Investigation, Formal analysis. **Rana Ghannam:** Writing – review & editing, Writing – original draft, Visualization, Validation, Methodology, Investigation, Formal analysis, Conceptualization. **Loic Coulomb:** Validation, Resources. **Romain Viennois:** Writing – review & editing, Writing – original draft, Visualization, Validation, Supervision, Resources, Methodology, Investigation, Formal analysis, Conceptualization. **Adrien Moll:** Writing – review & editing, Validation, Resources, Investigation, Formal analysis. **Mickael Beaudhuin:** Writing – original draft, Visualization, Validation, Supervision, Resources, Project administration, Methodology, Investigation, Funding acquisition, Formal analysis, Conceptualization.

Declaration of Competing Interest

The authors declare that they have no known competing financial interests or personal relationships that could have appeared to influence the work reported in this paper.

Data availability

Data will be made available on request.

Acknowledgement

We would like to thank the ANR-19-CE05-0001 for its financial support. The Raman and infrared experiments were performed on the IRaman Montpellier University platform.

Appendix A. Supporting information

Supplementary data associated with this article can be found in the online version at doi:10.1016/j.jallcom.2024.175422.

References

[1] J.P. Heremans, M.S. Dresselhaus, L.E. Bell, D.T. Morelli, When thermoelectrics reached the nanoscale, Nat. Nanotechnol. 8 (2013) 471–473. ⟨www.nature.com/naturenanotechnology⟩.
[2] J.R. Szczech, J.M. Higgins, S. Jin, Enhancement of the thermoelectric properties in nanoscale and nanostructured materials, J. Mater. Chem. 21 (2011) 4037–4055, https://doi.org/10.1039/c0jm02755c.
[3] T. Cao, X.L. Shi, M. Li, B. Hu, W. Chen, W.Di Liu, W. Lyu, J. MacLeod, Z.G. Chen, Advances in bismuth-telluride-based thermoelectric devices: progress and challenges, EScience 3 (2023) 100122, https://doi.org/10.1016/j.esci.2023.100122.
[4] W. Zhang, M. Li, Y. Zhang, Z. Tian, X.J. Li, H. Song, Re-optimising the thermoelectric properties of BiTeSe by CuO doping: from zone-melting ingots to powder metallurgy bulks with a large size, J. Alloy. Compd. 993 (2024) 174672, https://doi.org/10.1016/j.jallcom.2024.174672.
[5] M.I. Fedorov, G.N. Isachenko, Silicides: materials for thermoelectric energy conversion, Jpn. J. Appl. Phys. 54 (2015) 07JA05, https://doi.org/10.7567/JJAP.54.07JA05.
[6] A. Nozariasbmarz, A. Agarwal, Z.A. Coutant, M.J. Hall, J. Liu, R. Liu, A. Malhotra, P. Norouzzadeh, M.C. Öztürk, V.P. Ramesh, Y. Sargolzaeiaval, F. Suarez, D. Vashaee, Thermoelectric silicides: a review, Jpn. J. Appl. Phys. 56 (2017) 05DA04, https://doi.org/10.7567/JJAP.56.05DA04.
[7] M. Khalil, A. Moll, M. Godfroy, A. Letrouit-Lebranchu, B. Villeroy, E. Alleno, R. Viennois, M. Beaudhuin, Thermoelectric properties and stability of nanostructured chromium disilicide $CrSi_2$, J. Appl. Phys. 126 (2019) 135103, https://doi.org/10.1063/1.5117152.

[8] L. Abbassi, D. Mesguich, D. Berthebaud, S. Le Tonquesse, B. Srinivasan, T. Mori, L. Coulomb, G. Chevallier, C. Estournès, E. Flahaut, R. Viennois, M. Beaudhuin, Effect of nanostructuring on the thermoelectric properties of β-$FeSi_2$, Nanomaterials 11 (2021) 2852, https://doi.org/10.3390/nano11112852.

[9] M. Longhin, R. Viennois, D. Ravot, J.J. Robin, B. Villeroy, J.B. Vaney, C. Candolfi, B. Lenoir, P. Papet, Nanostructured CoSi obtained by spark plasma sintering, J. Electron. Mater. 44 (2015) 1963–1966, https://doi.org/10.1007/s11664-014-3611-6.

[10] S. Xia, H. Song, S. Liu, H. Hao, Low thermal conductivity and thermoelectric properties of $Si_{80}Ge_{20}$ dispersed $Bi_2Sr_2Co_2O_y$ ceramics, Ceram. Int. 49 (2023) 4707–4712, https://doi.org/10.1016/j.ceramint.2022.09.360.

[11] S. Le Tonquesse, W. Zhang, B. Srinivasan, B. Fontaine, T. Hiroto, T. Mori, J. F. Halet, D. Berthebaud, T.S. Suzuki, Improvement of thermoelectric properties via texturation using a magnetic slip casting process-the illustrative case of $CrSi_2$, Chem. Mater. 34 (2022) 1143–1156, https://doi.org/10.1021/acs.chemmater.1c03608.

[12] G.K. Goyal, S. Mukherjee, R.C. Mallik, S. Vitta, I. Samajdar, T. Dasgupta, High thermoelectric performance in $Mg_2(Si_{0.3}Sn_{0.7})$ by enhanced phonon scattering, ACS Appl. Energy Mater. 2 (2019) 2129–2137, https://doi.org/10.1021/acsaem.8b02148.

[13] Q. Zhang, L. Cheng, W. Liu, Y. Zheng, X. Su, H. Chi, H. Liu, Y. Yan, X. Tang, C. Uher, Low effective mass and carrier concentration optimization for high performance p-type $Mg_{2(1-x)}Li_{2x}Si_{0.3}Sn_{0.7}$ solid solutions, Phys. Chem. Chem. Phys. 16 (2014) 23576–23583, https://doi.org/10.1039/c4cp03468f.

[14] K. Singsoog, T. Seetawan, Effecting the thermoelectric properties of p-$MnSi_{1.75}$ and n-$Mg_{1.98}Ag_{0.02}Si$ module on power generation, Phys. B Condens. Matter 566 (2019) 1–5, https://doi.org/10.1016/j.physb.2019.02.052.

[15] Q. Guo, W. Zhang, Z. Liu, X. Fu, S. Le Tonquesse, N. Sato, H.W. Son, K. Shimamura, D. Berthebaud, T. Mori, Thermoelectric performance of Cr doped and Cr−Fe double-doped higher manganese silicides with adjusted carrier concentration and significant electron−phonon interaction, ACS Appl. Mater. Interfaces 13 (2021) 8574–8583, https://doi.org/10.1021/acsami.0c21484.

[16] Y. Miyazaki, D. Igarashi, K. Hayashi, T. Kajitani, K. Yubuta, Modulated crystal structure of chimney-ladder higher manganese silicides $MnSi_\gamma$ ($\gamma \sim 1.74$, Phys. Rev. B. 78 (2008) 214104, https://doi.org/10.1103/PhysRevB.78.214104.

[17] T. Homma, T. Kamata, N. Saito, S. Ghodke, T. Takeuchi, Effects of Re substitution for Mn on microstructures and properties in Re-substituted higher manganese silicide thermoelectric material, J. Alloy. Compd. 776 (2019) 8–15, https://doi.org/10.1016/j.jallcom.2018.10.209.

[18] R. Ghannam, A. Moll, D. Bérardan, L. Coulomb, A. Vieira-E-Silva, B. Villeroy, R. Viennois, M. Beaudhuin, Impact of the nanostructuring on the thermal and thermoelectric properties of α-$SrSi_2$, J. Alloy. Compd. 968 (2023) 171876, https://doi.org/10.1016/j.jallcom.2023.171876.

[19] A. Palenzona, M. Pani, The phase diagram of the Sr-Si system, J. Alloy. Compd. 373 (2004) 214–219, https://doi.org/10.1016/j.jallcom.2003.11.003.

[20] A. Garay, G. Trápaga, Z.K. Liu, R. Arróyave, Thermodynamic modeling of the Si-Sr system, Calphad Comput. Coupling Phase Diagr. Thermochem. 33 (2009) 550–556, https://doi.org/10.1016/j.calphad.2009.07.001.

[21] K. Li, S. Liu, C. Sha, Y. Du, A thermodynamic reassessment of the Si-Sr system, Calphad Comput. Coupling Phase Diagr. Thermochem. 35 (2011) 594–600, https://doi.org/10.1016/j.calphad.2011.09.007.

[22] Motoharu Imai, Sr–Si diagram at Si contents of 55–100 at% and crystal structure of $SrSi_{2-x}$, J. Alloy. Compd. 968 (2023) 172137.

[23] J. Evers, Transformation of three-dimensional three-connected silicon nets in $SrSi_2$, J. Solid State Chem. 24 (1978) 199–207, https://doi.org/10.1016/0022-4596(78)90010-5.

[24] M. Imai, T. Kikegawa, Phase transitions of alkaline-earth-metal disilicides MAESi2 (MAE = Ca, Sr, and Ba) at high pressures and high temperatures, Chem. Mater. 15 (2003) 2543–2551.

[25] Z.J. Chen, D.B. Tian, First-principles calculations of electronic, optical, and thermodynamic properties of $SrSi_2$, J. Appl. Phys. 109 (2011) 033506, https://doi.org/10.1063/1.3532031.

[26] M. Imai, T. Naka, T. Furubayashi, H. Abe, T. Nakama, K. Yagasaki, Electrical properties of polycrystalline $SrSi_2$, Appl. Phys. Lett. 86 (2005) 032102, https://doi.org/10.1063/1.1849423.

[27] B. Singh, G. Chang, T.-R. Chang, S.-M. Huang, C. Su, M.-C. Lin, H. Lin, A. Bansil, Tunable double-Weyl Fermion semimetal state in the $SrSi_2$ materials class, Sci. Rep. 8 (2018) 10540, https://doi.org/10.1038/s41598-018-28644-y.

[28] K. Manna, N. Kumar, S. Chattopadhyay, J. Noky, M. Yao, J. Park, T. Förster, M. Uhlarz, T. Chakraborty, B.V. Schwarze, J. Hornung, V.N. Strocov, H. Borrmann, C. Shekhar, Y. Sun, J. Wosnitza, C. Felser, J. Gooth, Three-dimensional quasiquantized Hall insulator phase in SrSi2, Phys. Rev. B. 106 (2022) L041113, https://doi.org/10.1103/PhysRevB.106.L041113.

[29] S.V. Ovsyannikov, V.V. Shchennikov, G.V. Vorontsov, A.Y. Manakov, A. Y. Likhacheva, V.A. Kulbachinskii, Giant improvement of thermoelectric power factor of Bi_2Te_3 under pressure, J. Appl. Phys. 104 (2008) 053713, https://doi.org/10.1063/1.2973201.

[30] W.T. Yen, K.K. Wang, H.J. Wu, Hybridization of n-type Bi_2Te_3 crystals with liquid-like copper chalcogenide elicits record-high thermoelectric performance, Mater. Today Phys. 34 (2023) 101065, https://doi.org/10.1016/j.mtphys.2023.101065.

[31] S.K. Singh, M. Imai, Thermoelectric properties of cubic Ba-substituted strontium disilicide, $Sr_{1-x}Ba_xSi_2$, with Ba content above solid solubility limit, Intermetallics 127 (2020) 106981, https://doi.org/10.1016/j.intermet.2020.106981.

[32] C.S. Lue, M.D. Chou, N. Kaurav, Y.T. Chung, Y.K. Kuo, Enhancement in the thermoelectric performance by Y substitution on $SrSi_2$, Appl. Phys. Lett. 94 (2009) 192105, https://doi.org/10.1063/1.3136847.

[33] M. Imai, A. Sato, T. Kimura, T. Aoyagi, Basic properties of $Sr_{1-x}Ba_xSi_2$, Thin Solid Films 519 (2011) 8496–8500, https://doi.org/10.1016/j.tsf.2011.05.040.

[34] A. Shende, A. Kore, P. Singh, First-principle based thermoelectric properties of Weyl semi-metal $SrSi_2$, AIP Conf. Proc. 2220 (2020) 130018, https://doi.org/10.1063/5.0001216.

[35] Y.K. Kuo, B. Ramachandran, C.S. Lue, Optimization of thermoelectric performance of $SrSi_2$-based alloys via the modification in band structure and phonon-point-defect scattering, Front. Chem. 2 (2014) 106, https://doi.org/10.3389/fchem.2014.00106.

[36] C.S. Lue, Y.S. Tseng, J.Y. Huang, H.L. Hsieh, H.Y. Liao, Y.K. Kuo, Low lattice thermal conductivity suppressed by Sr-deficiency in $Sr_{0.9}Ca_{0.1}Si_2$, AIP Adv. 3 (2013) 072132, https://doi.org/10.1063/1.4817576.

[37] K. Aoyama, T. Shimizu, H. Kuramochi, M. Mesuda, R. Akiike, T. Katase, Y. Kimura, H. Funakubo, Enhanced thermoelectric properties of $SrSi_2$ composite films with cubic and layered polymorphs, ACS Appl. Energy Mater. 6 (2023) 6593–6597, https://doi.org/10.1021/acsaem.3c00577.

[38] R. Ghannam, L. Coulomb, A. Moll, D. Bérardan, A. Vieira E Silva, B. Villeroy, R. Viennois, M. Beaudhuin, Enhanced thermoelectric properties of p-type α-$SrSi_2$ nanostructured by melt spinning, Solid State Sci. 147 (2024) 1–6, https://doi.org/10.1016/j.solidstatesciences.2023.107406.

[39] C.S. Lue, S.F. Wong, J.Y. Huang, H.L. Hsieh, H.Y. Liao, B. Ramachandran, Y.K. Kuo, Chemical pressure effect on thermoelectric properties of Ca and Ba substituted $SrSi_2$ alloys, J. Appl. Phys. 113 (2013) 013710, https://doi.org/10.1063/1.4772973.

[40] K. Aoyama, T. Shimizu, H. Kuramochi, M. Mesuda, R. Akiike, K. Ide, T. Katase, T. Kamiya, Y. Kimura, H. Funakubo, Thermoelectric $(Ba_xSr_{1-x})Si_2$ films prepared by sputtering method over the barium solubility limit, Jpn. J. Appl. Phys. 59 (2020) SFFB02, https://doi.org/10.7567/1347-4065/ab645b.

[41] J. Rodriguez-Carvajal, FULLPROF: a program for Rietveld refinement and pattern matching analysis, Satell. Meet. Powder Diffr. XV Congr. IUCr. 127 (1990).

[42] E. Alleno, D. Bérardan, C. Byl, C. Candolfi, R. Daou, R. Decourt, E. Guilmeau, S. Hébert, J. Hejtmanek, B. Lenoir, P. Masschelein, V. Ohorodnichuk, M. Pollet, S. Populoh, D. Ravot, O. Rouleau, M. Soulier, Invited Article: A round robin test of the uncertainty on the measurement of the thermoelectric dimensionless figure of merit of $Co_{0.97}Ni_{0.03}Sb_3$, Rev. Sci. Instrum. 86 (2015) 011301, https://doi.org/10.1063/1.4905250.

[43] X.F. Zheng, C.X. Liu, Y.Y. Yan, Q. Wang, A review of thermoelectrics research - Recent developments and potentials for sustainable and renewable energy applications, Renew. Sustain. Energy Rev. 32 (2014) 486–503, https://doi.org/10.1016/j.rser.2013.12.053.

[44] H.S. Kim, Z.M. Gibbs, Y. Tang, H. Wang, G.J. Snyder, Characterization of Lorenz number with Seebeck coefficient measurement, APL Mater. 3 (2015) 041506, https://doi.org/10.1063/1.4908244.

[45] G. Kresse, J. Furthmüller, Efficient iterative schemes for ab initio total-energy calculations using a plane-wave basis set, Phys. Rev. B - Condens. Matter Mater. Phys. 54 (1996) 11169–11186, https://doi.org/10.1103/PhysRevB.54.11169.

[46] D. Joubert, From ultrasoft pseudopotentials to the projector augmented-wave method, Phys. Rev. B Condens. Matter Mater. Phys. 59 (1999) 1758–1775, https://doi.org/10.1103/PhysRevB.59.1758.

[47] J.P. Perdew, K. Burke, M. Ernzerhof, Generalized gradient approximation made simple, Phys. Rev. Lett. 77 (1996) 3865–3868.

[48] M. Imai, Electrical resistivity of metastable phases of $BaSi_2$ synthesized under high pressure and high temperature, J. Alloy. Compd. 224 (1995) 111–116.

[49] K. Parlinski, Z.Q. Li, Y. Kawazoe, First-Principles Determination of the Soft Mode in Cubic ZrO_2, Phys. Rev. Lett. 78 (1997) 4063–4066.

[50] J. Evers, G. Oehlinger, A. Weiss, Solid solutions $M_{1-x}Sr_xSi_2$ (M = Ca, Eu, Ba) and $BaSi_{2-y}Ge_y$ with $SrSi_2$-type structure, J. Less Common Met. 69 (1980) 399–402, https://doi.org/10.1016/0022-5088(80)90299-4.

[51] A. Moll, M. Beaudhuin, V. Legrand, R. Debord, S. Pailhès, R. Viennois, N. Fréty, Mechanical alloying as a new synthesis route for metastable silicon clathrates, Mater. Lett. 187 (2017) 1–3, https://doi.org/10.1016/j.matlet.2016.10.053.

[52] M. Khalil, M. Beaudhuin, B. Villeroy, D. Ravot, R. Viennois, A modeling approach for new $CrSi_2$ based alloys: application to metastable $Cr_{1-x}Zr_xSi_2$ as a potential thermoelectric material, J. Alloy. Compd. 662 (2016) 150–156, https://doi.org/10.1016/j.jallcom.2015.12.048.

[53] S.A. Hassanzadeh-Tabrizi, Precise calculation of crystallite size of nanomaterials: a review, J. Alloy. Compd. 968 (2023) 171914, https://doi.org/10.1016/j.jallcom.2023.171914.

[54] José Flores Livas, Computational and Experimental Studies of sp3-Materials at High Pressure, 1, Université de Lyon, 2012.

[55] R. Viennois, P. Toulemonde, Raman scattering study of the lattice dynamics of the narrow-gap semiconducting alkaline-earth disilicide, : Int. Conf. Narrow Gap Semicond. (2006) 235.

[56] R. Ghannam, Approche multi-échelle pour l'optimisation des propriétés thermoélectriques du disiliciure de strontium, Université de Montpellier (2023).

[57] H.J. Goldsmid, Introduction to Thermoelectricity (2016), https://doi.org/10.1533/9781845690915.3.339.·.